Elucidation of Mass Transport Phenomena in Highly Concentrated Electrolytes during Current Cycling Using In-Situ Interferometry and Finite Difference Method

Journal of The Electrochemical Society, 2024 **171** 040519
1945-7111/2024/171(4)/040519/8/$40.00 © 2024 The Electrochemical Society ("ECS"). Published on behalf of ECS by IOP Publishing Limited

Elucidation of Mass Transport Phenomena in Highly Concentrated Electrolytes during Current Cycling Using In-Situ Interferometry and Finite Difference Method

Go Kamesui,[1] Kei Nishikawa,[2,3,*] Mikito Ueda,[1,*] and Hisayoshi Matsushima[1,*,z]

[1]*Faculty of Engineering, Hokkaido University, Kita 13 Nishi 8, Sapporo, Hokkaido 060-8628, Japan*
[2]*Rechargeable Battery Materials Group, Center for Green Research on Energy and Environmental Materials, National Institute for Materials Science, 1-1 Namiki, Tsukuba, Ibaraki 305-0044, Japan*
[3]*Center for Advanced Battery Collaboration, Center for Green Research on Energy and Environmental Materials, National Institute for Materials Science, 1-1 Namiki, Tsukuba, Ibaraki 305-0044, Japan*

Understanding electrolyte mass transfer during charge–discharge reactions is essential for developing next-generation storage batteries with high energy densities. In this study, we investigated Li^+ transport in a highly concentrated electrolyte (HCE) consisting of an equimolar mixture of lithium bis(fluorosulfonyl)amide (LiFSA) and tetraglyme (G4) under current reversal and re-reversal. Concentration profiles of the electrolyte at a distance of 0–600 μm from the Li electrodes were obtained using in situ laser interferometry. The Li^+ transference numbers and LiFSA diffusion coefficients were calculated from these profiles. Raman spectroscopy suggested that the coordination structure surrounding Li^+ ions in the electrolytes mainly contributed to the transference number. A one-dimensional unsteady diffusion equation and the finite difference method were employed to simulate the concentration profiles. The maximum error percentage between the measured and simulated values was only 3%, confirming the accuracy and validity of the interferometric measurements. Our findings on Li-ion transfer in HCEs could promote the rational design of high-energy-density Li-ion batteries with higher cation transference numbers of electrolytes and charge–discharge rates.
 [DOI: 10.1149/1945-7111/ad3ad1]

Manuscript submitted February 7, 2024; revised manuscript received March 21, 2024. Published April 15, 2024.

Supplementary material for this article is available online

Lithium-ion batteries (LIBs) exhibit high energy densities, owing to which they are widely utilized in various devices, such as smartphones and laptops. As the demand for smart grids powered by renewable energy and electric vehicles (EVs) continues to grow, developing suitable storage batteries has become crucial. Previous studies have shown that LIBs have nearly reached their theoretical capacity.[1–4] Hence, LIBs with higher energy densities should be developed. Moreover, the development of high-speed charge–discharge properties is necessary for the efficient operation of EVs. A key factor influencing the charge–discharge rate of storage batteries is the cation transference number of the electrolyte (t^+).[5] The higher t^+ is, the lower the concentration polarization of the electrolyte becomes, which enables faster charge–discharge reactions. Therefore, it is crucial to explore and identify electrolytes with high t^+.

One approach to increasing the energy density involves increasing the electrolyte concentration. In 2010, Watanabe et al. discovered that an equimolar mixture of Li salt and glyme solvent showcased a wide potential window and strong resistance to thermal decomposition, which was attributed to the chelating effect.[6] This solution exhibited similar properties to those of ionic liquids and was named a solvate ionic liquid (SIL).[7] In 2014, Yamada et al. and Sodeyama et al. observed that ultra-high-concentration acetonitrile electrolytes over 4 mol L^{-1} exhibited significantly higher resistance to reductive decomposition than commercial electrolytes of approximately 1 mol L^{-1}.[8,9] Highly concentrated electrolytes (HCEs), including SIL, have a unique solvation structure in which almost all solvent molecules are coordinated to cations. This structure enables the HCE to achieve operating voltages in the 4–5 V range,[10] thereby increasing the battery's energy density. Notably, HCEs also exhibit high t^+.[11,12] Typically, a tradeoff exists between the t^+ value and the ionic conductivity of the electrolyte. However, the cations in a HCE are transported via a hopping mechanism between salt-solvent clusters, resulting in high ionic conductivity despite their high viscosity.[13]

Metallic Li has the lowest density (0.534 g cm^{-3}) and the most negative electrode potential (−3.04 V vs standard hydrogen electrode) among all metals.[14] Additionally, it exhibits a significantly high theoretical capacity of 3860 mAh g^{-1}, making it an ideal candidate for enhancing the energy density of batteries.[15] Li-sulfur batteries[16] and Li-air batteries[17] have also been developed with metallic Li as the negative electrode. However, whisker- or dendrite-like Li deposits appeared on the electrodes during the charge (electrodeposition) and discharge (electrochemical dissolution) reactions. These sharp Li deposits may pierce the separator within the battery, resulting in potential short circuits and ignition accidents. Therefore, the practical application of Li metal as a negative electrode has not yet been achieved.

Mass transport in electrolytes during electrochemical reactions relies on three mechanisms: diffusion, migration, and convection.[18] When an electrochemical reaction is initiated, the concentration of metal ions near the electrode changes, creating a concentration gradient that drives the diffusion of the ionic species.[19] Electrolysis forms a potential gradient between the electrodes in the electrolyte, causing anions to migrate toward the anode and cations toward the cathode.[20] Additionally, the density difference between the bulk and electrolyte close to the electrode triggers natural convection, further enhancing mass transport.[21] Transporting metal ions from the bulk to the cathode surface is vital for understanding metal electrodeposition.[22] The rate of Li electrolysis in organic electrolytes is significantly influenced by Li^+ transport near the cathode.[23,24] An inadequate Li^+ supply to the cathode surface leads to Li^+ depletion, resulting in an uneven morphology of Li deposition. Hence, understanding the Li^+ transport mechanism in the electrolyte is vital for controlling the morphology of Li deposition. Furthermore, we previously reported that the Li^+ diffusion from the anode surface to the bulk in sulfolane-based HCE governs the electrolysis speed at 5 mA cm^{-2}.[25] Consequently, a thorough understanding of the Li^+ mass transfer in electrolytes near both electrodes is essential for applying Li electrodes and HCE in storage batteries.[26,27] However, thus far, such investigations have focused on charging processes, specifically related to Li electrodeposition.[25,28–34] In actual rechargeable batteries, discharging occurs after charging. During discharging, Li^+ ions move in the opposite direction to that during charging, potentially affecting the Li deposition-dissolution mechanism.

*Electrochemical Society Member.
[z]E-mail: matsushima@eng.hokudai.ac.jp

Therefore, understanding electrolyte mass transfer during current cycling is crucial to controlling Li deposition's morphology.

We previously used in situ laser interferometry to observe the concentration distribution near an electrode during electrochemical reactions using lithium bis(trifluoromethanesulfonyl)amide or lithium bis(fluorosulfonyl)amide (LiFSA) and tetraglyme (G4) SILs.[19,31] Laser interferometry, a technique first employed by McLarnon et al. in the 1970s,[35,36] has been widely adopted in numerous studies.[25,31,37–41] Interferometers can detect changes in the refractive indices of the electrolytes. In the case of a solute-solvent binary electrolyte, the refractive index directly corresponds to the concentration of the solute. Hence, information regarding the change in electrolyte concentration can be obtained by detecting changes in the refractive index.

In this study, the concentration changes in a highly concentrated electrolyte (an equimolar mixture of LiFSA and G4) between the Li electrodes were observed using in situ laser interferometry under current reversal and re-reversal. The Li^+ transference number and LiFSA diffusion coefficient were obtained from the concentration profiles using the pseudo-Hittorf method. Raman spectroscopy determined the relationship between the Li^+ solvation structure and the transference number. The concentration distribution during electrolysis was simulated using a one-dimensional unsteady diffusion equation to validate the concentration profiles obtained using interferometry. Furthermore, the approximate concentration profiles during current reversal and re-reversal were estimated using the finite difference method (FDM)[42,43] to verify the results obtained by interferometry.

Experimental

Schematics of an overview and cross-sectional view of the experimental cell are presented in Figs. 1a and 1b, respectively. Note that the electrode that was the anode during electrolysis is denoted as Electrode A and the one that was the cathode as Electrode B. The entire setup, including the experimental cell and electrolyte, was prepared in a dry room with a dew point below −50 °C. The anode and cathode were Li foil (99.9%, Honjo Metal, Japan). The reaction area of both electrodes was 200 μm (length) × 15 mm (width). To create the electrolyte, a mixture of LiFSA (99.9%, Nippon Shokubai Co., Ltd) and G4 (98%, Kishida Chemical Co., Ltd) in varying molar ratios was used. This mixture was placed on a hot plate at 50 °C overnight to ensure complete dissolution. The relationship between the LiFSA: G4 molar ratio and LiFSA concentration is shown in Table I. For the current collector, a 5 μm thick Cu foil was employed. During the assembly of the experimental cell, the current collector was placed on a glass slide, and the Li electrode was positioned on top of it. The electrode surfaces were arranged in a quasi-two-dimensional configuration with parallel orientation to minimize the effect of natural convection. The inter-electrode distance between the two electrodes was maintained at 600 μm. Subsequently, a 15 mm wide glass slide was placed over both electrodes and secured with epoxy resin along its edges. The electrolyte was injected between both electrodes. The electrochemical experiment was started after sealing the inlet to prevent contact with air.

All experiments were conducted at room temperature (23 °C). The refractive index and density of the electrolyte were obtained from a previous study.[19] Current application was performed using a potentiostat (HZ-Pro S12, Hokuto Denko, Japan). The current density was set to 3 mA cm^{-2} and was applied to the experimental cell in different directions every 100 s. The correspondence between the current application's direction and the electrode type is shown in Table II.

A digital holographic interferometer (DHM T1000, Lyncée Tec, Switzerland) was employed to monitor the change in the concentration distribution of LiFSA in the electrolyte between the two electrodes during current application. The laser light had a wavelength of 683.6 nm. The optical path length was 200 μm, which was consistent with the electrode thickness. Holograms obtained by DHM were analyzed using Koala software (Lyncée Tec) to calculate concentration profiles.[25,31,41] The refractive index of the electrolyte is proportional to the concentration;

$$\Delta n = \left(\frac{\partial n}{\partial C}\right)\Delta C \qquad [1]$$

where Δn is the change in refractive index, and ΔC is the change in LiFSA concentration. The interference equation can be expressed as in Eq. 2;

$$d\Delta n = \left(\frac{\Delta\theta}{2\pi}\right)\lambda \qquad [2]$$

where d is the optical path length, $\Delta\theta$ is the phase change of the electrolyte, and λ is the wavelength of the laser light. From Eqs. 1 and 2, we obtain Eq. 3;

$$\Delta C = \left(\frac{\partial C}{\partial n}\right)\left(\frac{\Delta\theta}{2\pi}\right)\left(\frac{\lambda}{d}\right) \qquad [3]$$

If the interferometer observes the electrolyte and detects $\Delta\theta$ during electrolysis, the ΔC associated with Li electrodeposition/-chemical dissolution can be calculated. The relationship between $\Delta\theta$ and ΔC is shown in Fig. 2.

The Raman spectra of the electrolyte were measured with a laser micro-Raman spectrometer (LabRAM 1B, HORIBA, Japan). The wavelength of the excitation laser was 632.7 nm. The resolution of the spectrometer was about 1 cm^{-1}. The exposure time and cumulative exposures were 15 s and 4 times, respectively.

Results and Discussions

Electrolysis.—Movie S1 shows the real-time observation of the LiFSA concentration change in the LiFSA-G4 equimolar electrolyte during electrolysis. The color change represents the phase change of the electrolyte. Figure 3 shows the changes in the concentration of LiFSA in the LiFSA-G4 equimolar electrolyte during electrolysis. The horizontal dotted line represents the initial LiFSA concentration

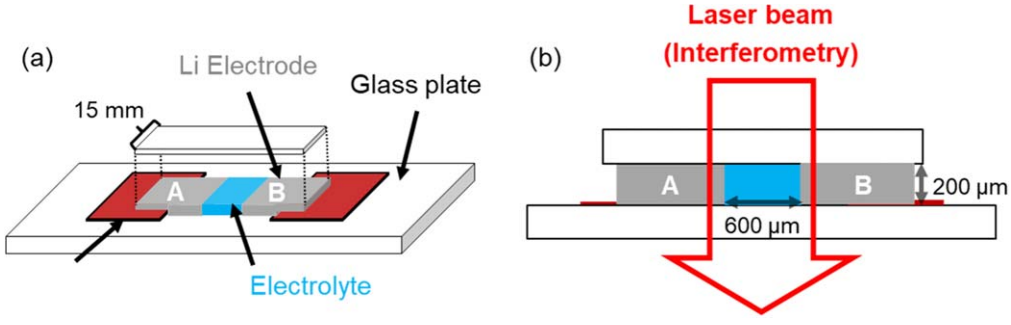

Figure 1. Schematic of the (a) overview and (b) cross-sectional view of the experimental cell.

Table I. Relationship between LiFSA: G4 molar ratio and LiFSA concentration in the electrolyte.

LiFSA: G4 molar ratio, $M_{LiFSA/G4}$/mol mol^{-1}	LiFSA concentration, C_e/mol l^{-1}
0.6: 1	2.23
0.7: 1	2.52
0.8: 1	2.78
0.85: 1	2.91
0.9: 1	3.03
1.0: 1	3.27
1.1: 1	3.48
1.15: 1	3.59
1.2: 1	3.69
1.3: 1	3.89
1.4: 1	4.08
1.5: 1	4.26

Table II. Relationship between the direction of current application and the type of electrodes.

	Electrolysis (0–100 s)	Current reversal (100–200 s)	Current re-reversal (200–300 s)
Electrode A	Anode	Cathode	Anode
Electrode B	Cathode	Anode	Cathode

in the electrolyte (C_e = 3.27 mol L^{-1}). During electrolysis, the LiFSA concentration at the anode surface increased and reached 3.69 mol L^{-1} after 100 s. This concentration increase formed a negative concentration gradient near the anodes. Consequently, the diffusion layer, which is more concentrated than the bulk, became thicker. In contrast, LiFSA concentration at the cathode surface decreased during electrolysis, reaching 2.90 mol L^{-1} after 100 s. This concentration change created a negative concentration gradient near the cathode, expanding the thickness of diffusion layer with a lower concentration than the bulk. Figure S2 shows the concentration profiles at (a) C_e = 2.52 and (b) 3.89 mol L^{-1}. In both cases, the LiFSA concentration near the anode increased, and that near the cathode decreased as the electrolysis proceeded over time.

Figures S3(a) and S3(b) show the Raman spectra of the LiFSA powder, G4, and solutions with various LiFSA concentrations at 700–800 cm^{-1}. Fujii et al. and Yoon et al. reported that S–N–S stretching vibrations of uncoordinated FSA^- appear at 720–730 cm^{-1}.[44,45] The peaks in the spectra shifted toward higher wavenumbers as C_e increased, suggesting the increase in the number of contact ion pairs (CIPs) and aggregates (AGGs) at Li^+ and FSA^-.[46] Figures S3(c) and S3(d) show the Raman spectra of the LiFSA powder, G4, and solutions with various LiFSA compositions at 800–900 cm^{-1}. Grondin et al. reported that the C–O stretching and CH_2 locking vibrations of G4 appear at 800–900 cm^{-1}.[47] The peak intensity at 870 cm^{-1} increased for $C_e \leqslant$ 3.27 mol L^{-1},

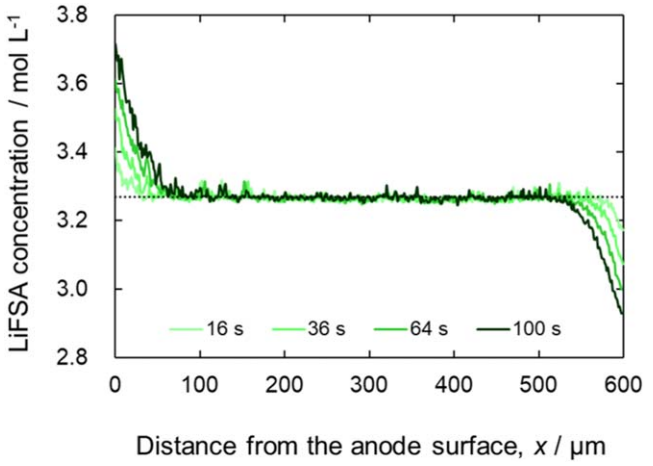

Figure 3. Concentration profile of lithium bis(fluorosulfonyl)amide (LiFSA) during electrolysis in an equimolar mixture of LiFSA and tetraglyme (LiFSA-G4) electrolytes.

reaching maximum intensity at C_e = 3.27 mol L^{-1}. This suggests that the proportion of G4 solvated with Li^+ in solution increases with increasing C_e. In contrast, the peak intensity decreased for $C_e \geqslant$ 3.27 mol L^{-1}. The differences in peak positions and peak intensities of the spectra across various C_es are consistent with the previous work by Terada et al.[48] Tsuzuki et al. reported that the energy level of the highest occupied molecular orbital of G4 was elevated in the cation-G4-TFSA complex compared to the cation-G4 complex.[49] Consequently, an excess of LiFSA can influence the formation of complexes between Li^+ and G4.[31]

The concentration profiles after 100 s were integrated against the x-axis to calculate the change in the LiFSA concentration from that before electrolysis (denoted by α) near each electrode. α was then used to determine t^+ using the pseudo-Hittorf method (see Supporting Information S2). Figure 4a shows t^+ values for electrolytes with different C_e. t^+ increased with increasing C_e. This tendency is consistent with the results of Fawdon et al., who measured the t^+ values of LiFSA-G4 solutions below 2 mol L^{-1}.[50] Li^+ was solvated by G4 at low C_e, thereby increasing the Stokes radius. However, FSA^- has weak interactions with Li^+, resulting in a smaller Stokes radius and higher mobility than Li^+. CIPs and AGGs were formed in the solution with increasing C_e (Fig. 4b). These complexes decrease the mobility of FSA^- with Li^+,[51] thus increasing t^+ as C_e increases. Typically, the partial molar volume of the solute (V_e) increases with increasing solute concentration in the electrolyte.[32,50] However, increased cation-G4-FSA complexation due to increasing C_e would compress LiFSA, thus decreasing V_e (Fig. S1(c)). Terada and Ueno et al. have previously measured t^+ of Li^+ in an equimolar mixture of LiFSA-G4 using pulsed-gradient spin-echo nuclear magnetic resonance spectroscopy (PGSE-NMR), obtaining a value of 0.44.[48,52] This value does not significantly deviate from the range of 0.51–0.53 that we obtained through pseudo-Hittorf experiments.

Figure 4c shows the C_e dependency of the apparent LiFSA diffusion coefficient (D), as determined by Eqs. S9 and S10. D

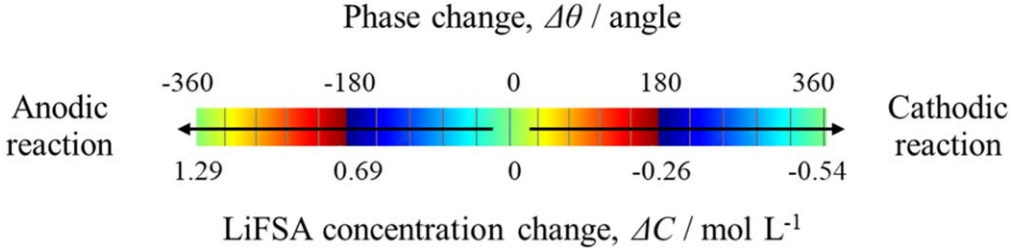

Figure 2. The relationship between the phase change and the LiFSA concentration change. Reproduced with permission from[19].

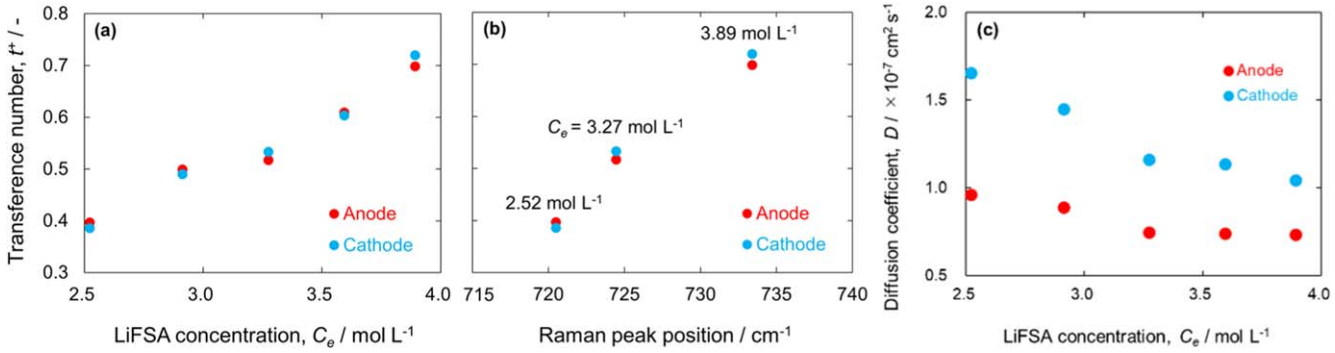

Figure 4. (a) Li^+ transference number near the anode and cathode; (b) relationship between Raman peak position and Li^+ transference number; and (c) diffusion coefficient near the anode and cathode at various electrolyte concentrations.

decreased with increasing C_e. Typically, an inversely proportional relationship exists between the electrolyte viscosity and the diffusion coefficient.[18] We observed that the viscosity of the electrolyte increased with increasing C_e,[19] which explains the decrease in D. Furthermore, D was more significant at the cathode than at the anode, which is the same as the results of our previous studies.[19,25,31] During electrolysis, the LiFSA concentration increases near the anode and decreases near the cathode. Consequently, the electrolyte near the anode exhibits a higher viscosity than that near the cathode, resulting in a difference in D between the two electrodes.

Terada et al. have previously reported the self-diffusion coefficient (D_{self}) of each species in electrolytes, comprising various ratios of LiFSA and G4, using pulsed field gradient-NMR.[48] They observed a decrease in D_{self} for all chemical species as C_e increased. The D_{self} for Li^+ and FSA^- were approximately close to the Ds we calculated. Furthermore, for $M_{LiFSA/G4} > 1$, the D_{self} of FSA^- becomes 2–5 times greater than that of Li^+. However, the single-wavelength interferometry method we used could only observe the transport phenomena of a single component, preventing us from discerning the differences in diffusion coefficients among ion species.

Figure 5a shows the theoretically calculated concentration profile of LiFSA-G4 equimolar electrolytes during electrolysis. The changes in the concentration profile every 1 s are shown in Fig. S5 (a). Equation 4 (anode) and 5 (cathode), derived from the Laplace transform of Fick's second law, were employed to calculate the theoretical concentration profiles;

$$C(x,t) = C_e + \frac{i(1-t^+)}{zFD}(1 - C_e V_e)\left[2\sqrt{\frac{Dt}{\pi}}\exp\left(-\frac{x^2}{4Dt}\right) - x \quad erfc\left(\frac{x}{\sqrt{4Dt}}\right)\right] \quad [4]$$

$$C(x,t) = C_e - \frac{i(1-t^+)}{zFD}(1 - C_e V_e) \times \left[2\sqrt{\frac{Dt}{\pi}} \quad \exp\left(-\frac{(L-x)^2}{4Dt}\right) - x \quad erfc\left(\frac{L-x}{\sqrt{4Dt}}\right)\right] \quad [5]$$

where C is the LiFSA concentration in the electrolyte, x is the distance from the anode surface, t is the time, z is the valence, F is the Faraday constant, i is the current density, V_e is the partial molar volume of LiFSA, and L is the inter-electrode distance (for the derivation of the equation, see Supporting Information S1). The error between the concentration profile obtained via interferometry and the theoretical value is shown in Fig. 5b. The maximum divergence is 1.8%. These results validate the electrolyte concentration profiles measured using interferometry.

Figure 6 shows the ion movement in LiFSA-G4 equimolar electrolytes before and during electrolysis. The dotted line represents the concentration boundary between the diffusion layer and the bulk.

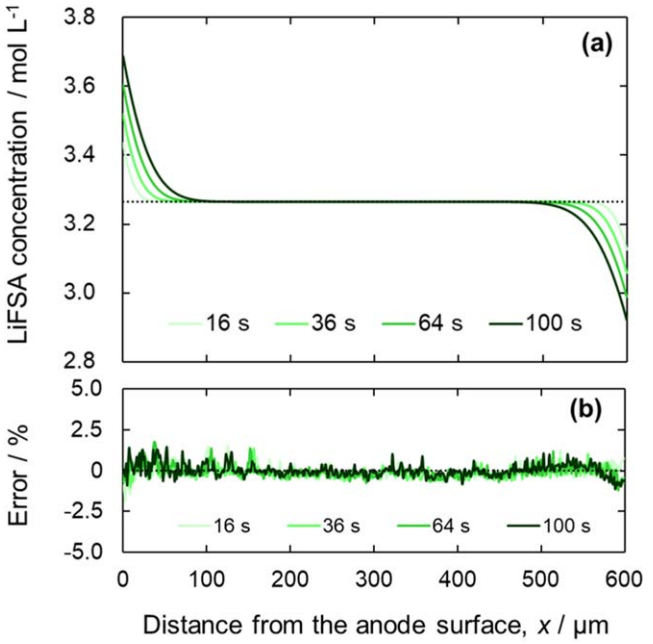

Figure 5. (a) Theoretically calculated concentration profile of LiFSA in LiFSA-G4 equimolar electrolyte during electrolysis and (b) error between the measured and theoretical concentration profiles.

Before the electrolysis, the ions are uniformly distributed in the electrolyte. However, Li^+ moves from the anode surface to the electrolyte during electrolysis and is consumed at the cathode surface. Moreover, Li^+ and FSA^- migrate in the presence of an excess positive charge near the cathode to maintain the macroscopic electroneutrality of the electrolyte. As $t^+ \approx 0.5$ at C_e = 3.27 mol L^{-1}, Li^+ and FSA^- migrate in equal numbers—similarly, excess negative charge at the cathode surface results in ion migration to maintain electrical neutrality. Hence, ion migration balances the charges at both electrodes, increasing or decreasing the ion concentration in the electrolyte at the anode and cathode compared to that in the bulk. Finally, LiFSA diffuses owing to the concentration difference between the two electrode surfaces and the bulk. Figures S2(c) and S2(d) show the ion movement in electrolytes during electrolysis at $C_e < 3.27$ and $C_e > 3.27$ mol L^{-1}. For $C_e <$ 3.27 mol L^{-1}, FSA^- migrated more than Li^+ as $t^+ < 0.5$, whereas for $C_e > 3.27$ mol L^{-1}, Li^+ migrated more than FSA^- as $t^+ > 0.5$.

Current reversal.—Figure 7a shows the LiFSA concentration profiles in the LiFSA-G4 equimolar electrolyte at reversed applied

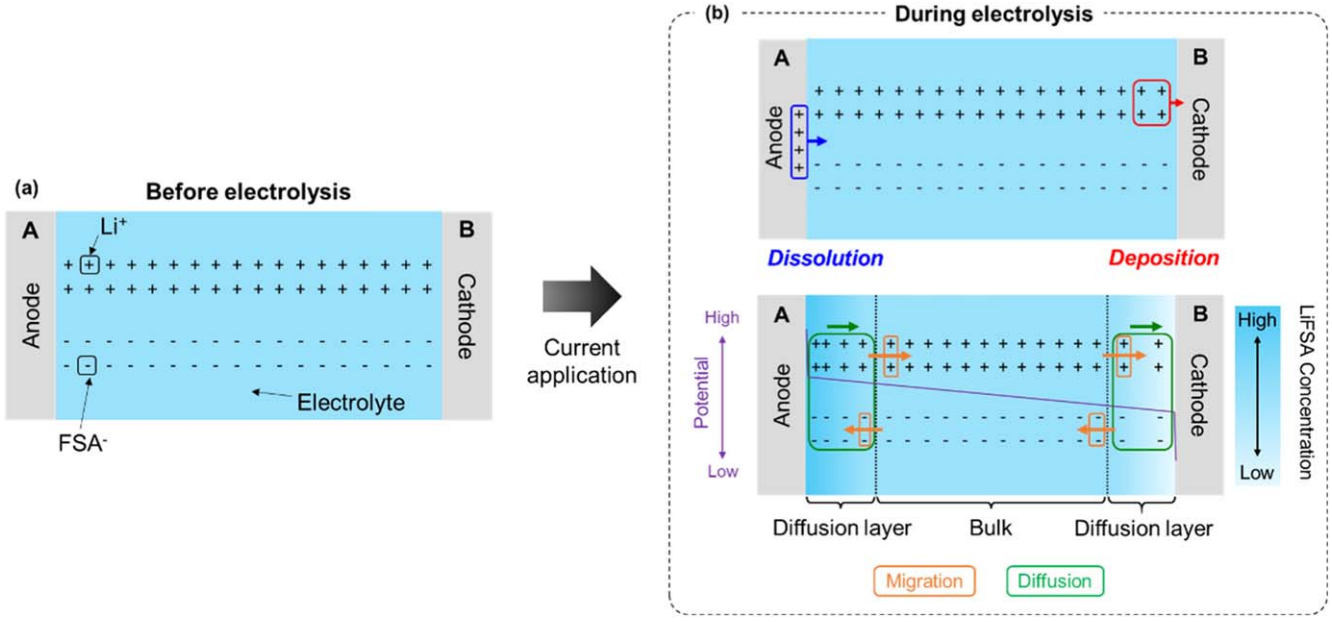

Figure 6. Schematics of the ion movement (a) before and (b) during electrolysis in LiFSA-G4 equimolar electrolyte.

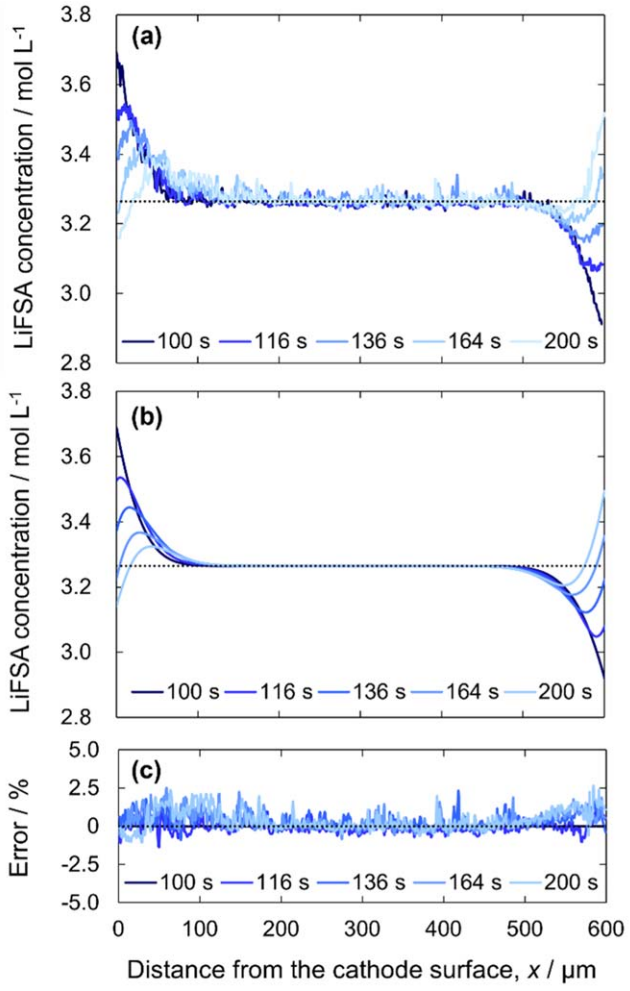

Figure 7. LiFSA concentration profile in LiFSA-G4 equimolar electrolyte during current reversal obtained by (a) interferometry and (b) finite difference method (FDM); (c) error between the concentration profiles of interferometry and FDM.

current. The legends indicate the time elapsed since the beginning of electrolysis. The current reversal exchanged the anode and cathode for electrolysis. The Li concentration on the cathode surface, which had been higher than the bulk, decreased during electrodeposition, reaching 3.16 mol L^{-1} after 200 s. An upward convex concentration gradient formed near the cathode owing to the change in the Li concentration at the cathode surface; after 200 s, a positive concentration gradient was observed at 0–50 μm from the cathode surface and a negative gradient at 50–120 μm. In contrast, at the anode, where the concentration had been lower than the bulk, the electrodeposition increased with Li dissolution, reaching 3.51 mol L^{-1} after 200 s. This change resulted in a downward convex concentration gradient at the anode, in contrast to that near the cathode. After 200 s, a negative concentration gradient was observed at 470–550 μm from the cathode surface and a positive gradient at 550–600 μm. Figure 7b shows the FDM Li concentration profiles in a LiFSA-G4 equimolar electrolyte during current reversal (see Supporting Information S4). The FDM-estimated concentration changes for every 1 s are shown in Fig. S5(b). Almost symmetrical upward and downward convex profiles are observed. After 200 s, the inflection point of the concentration gradient was identified at nearly the same position as that obtained via interferometry. Figure 7c shows the error between the concentration profiles obtained by interferometry and FDM. The maximum deviation was 2.5%, confirming the validity of the concentration profile obtained by interferometry during the current reversal. This also indicates the accuracy of the interferometric measurements.

Figures 8a and 8b show the ion movement in the LiFSA-G4 equimolar electrolyte before and after current reversal. We assumed that t^+ remained constant at approximately 0.5 during current cycling. The concentration gradient formed during electrolysis before current reversal was maintained until the end of the electrolysis. Therefore, Li^+ and FSA^- near both electrodes diffused from the anode to the cathode. The direction of the applied current was reversed immediately after electrolysis was complete. When an excess negative charge existed near the cathode owing to Li^+ consumption at the cathode surface, Li^+ and FSA^- migration maintained macroscopic electrical neutrality near the cathode. Subsequently, the LiFSA concentration at 0–50 μm from the cathode surface decreased, forming an upward convex concentration gradient near the cathode. In contrast, when an excess positive charge existed near the anode owing to the Li^+ supply at the anode surface, ion

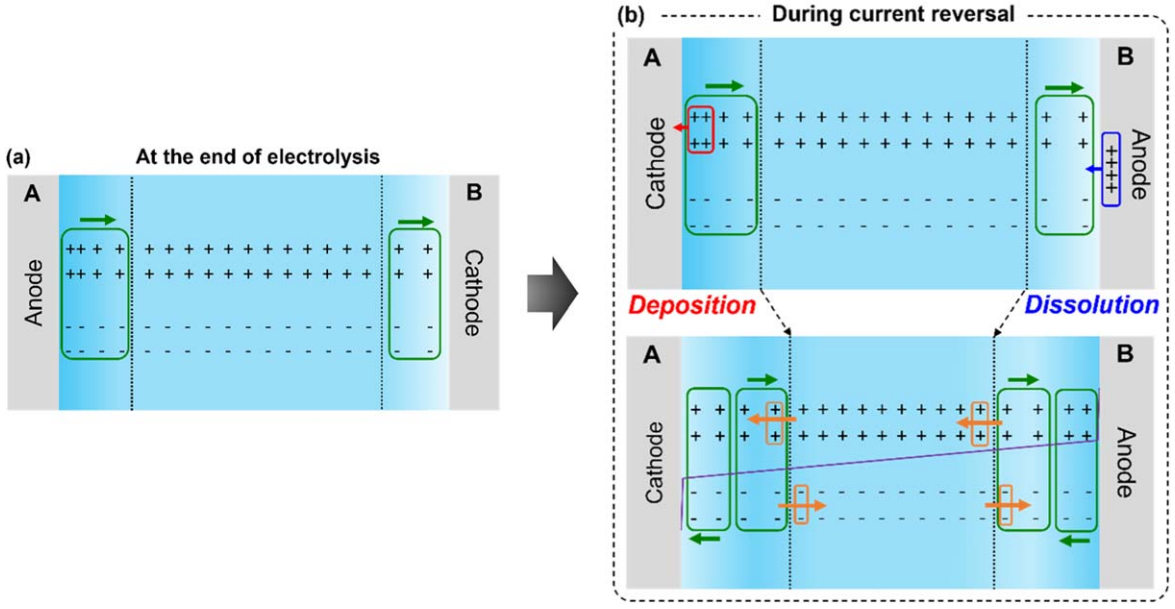

Figure 8. Schematics of ion movement in the electrolyte (d) before and (e) after current reversal.

migration maintained electrical neutrality near the anode. Then, the LiFSA concentration at 550–600 μm from the cathode surface increased, forming a downward convex concentration gradient near the anode.

Figure 9a shows the concentration profile of the LiFSA-G4 equimolar electrolyte when the direction of the applied current was reversed again. The current re-reversal exchanges the anode and cathode again. The Li concentration increased at the anode and decreased at the cathode, reaching 3.67 and 2.95 mol L^{-1} after 300 s, respectively. With this change, the convex concentration gradient formed during the current reversal gradually transformed into a negative gradient. Compared to the first electrolysis step, the electrode surface concentration changed less from the bulk concentration at 300 s than at 100 s. This is because the electrode surface concentration approached the bulk concentration due to the reversal of the current before the current reversal. Figure 9b shows the FDM estimate of the electrolyte concentration profile during current re-reversal. The concentration changes obtained at 1 s intervals are shown in Fig. S5(c). The convex concentration gradients near both electrodes, formed by current reversal, were all unified downward, consistent with interferometry. Figure 9c shows the error between the concentration profiles obtained by interferometry and FDM. The maximum deviation was 2.6%, confirming the validity of the concentration profile of the electrolyte during current re-reversal by interferometry.

Figures 10a and 10b show the ion movement in the LiFSA-G4 equimolar electrolyte before and after current re-reversal. Before the applied current direction was reversed again, the electrolyte maintained an upward and downward convex concentration gradient formed by the current reversal. Hence, two different directions of LiFSA diffusion existed near both electrodes—one approaching the anode and the other approaching the cathode. Upon reversing the direction of the applied current again, Li^+ is supplied from the anode surface to the electrolyte because of Li dissolution. Simultaneously, Li^+ is consumed from the electrolyte on the cathode surface via Li deposition. When an excess positive charge exists near the anode

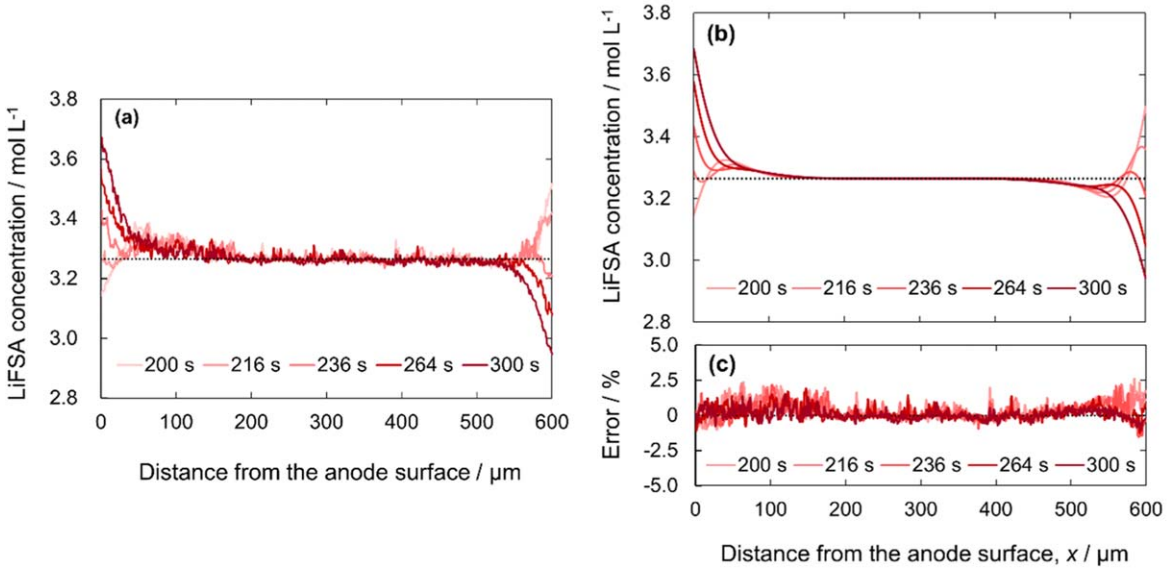

Figure 9. LiFSA concentration profile during re-reversal of the applied current in the LiFSA-G4 equimolar electrolyte obtained by (a) interferometry and (b) FDM; (c) error of concentration profiles between interferometry and FDM.

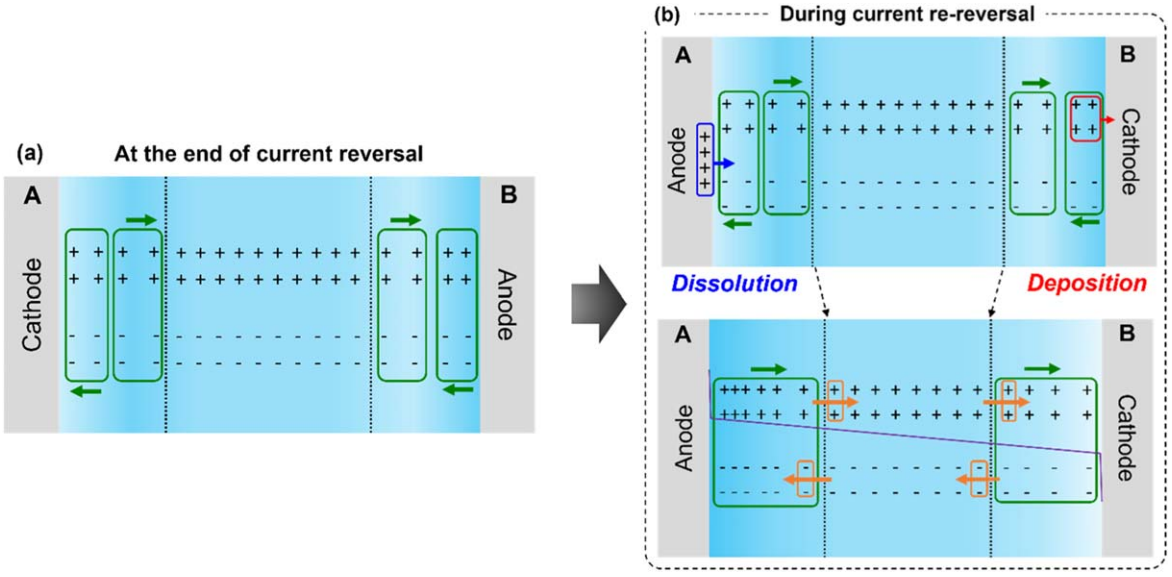

Figure 10. Schematics of ion movement in the electrolyte (a) before and (b) after current re-reversal.

and an excess negative charge exists near the cathode, the migration of ionic species maintains the electrical neutrality of the electrolyte. Hence, the LiFSA concentration increased near the anode and decreased near the cathode. Consequently, the upward and downward convex concentration gradients unified into a negative gradient during the current re-reversal.

Conclusions

In this study, we used in situ interferometry to observe the concentration profile of the electrolyte containing an equimolar mixture of lithium bis(fluorosulfonyl)amide and tetraglyme (LiFSA-G4) during current cycling. We investigated the mass transfer mechanism during electrochemical reactions. The Li^+ transference number increased with increasing electrolyte concentration because of the coordinated structure surrounding the Li^+. The LiFSA diffusion coefficient decreased with increasing electrolyte concentration due to increased viscosity. When the concentration profile was estimated using the finite difference method (FDM), the maximum percentage error between the measured and approximate values was 2.6%. This indicates that FDM is a reliable tool for estimating the concentration profile during cycling. A thorough understanding of the mass transfer mechanism in electrolytes is crucial to enhancing the energy density of storage batteries with HCE and Li electrodes. This study represents a milestone toward realizing next-generation high-energy-density storage batteries.

Acknowledgments

This work was partly supported by a Japan Science and Technology Agency COI-NEXT grant (grant number JPMJPF2016) and JSPS KAKENHI (grant number JP20H00399 and 23KJ0054).

ORCID

Go Kamesui https://orcid.org/0009-0003-1969-5578
Kei Nishikawa https://orcid.org/0000-0002-7718-7606
Mikito Ueda https://orcid.org/0000-0003-2068-1715
Hisayoshi Matsushima https://orcid.org/0000-0001-8612-7640

References

1. J. M. Tarascon and M. Armand, *Nature*, **414**, 359 (2001).
2. J. B. Goodenough and Y. Kim, *Chem. Mater.*, **22**, 587 (2010).
3. P. K. Nayak, L. Yang, W. Brehm, and P. Adelhelm, *Angew. Chem. Int. Ed.*, **57**, 102 (2018).
4. Y. Tian et al., *Chem. Rev.*, **121**, 1623 (2021).
5. E. R. Logan and J. R. Dahn, *Trends Chem.*, **2**, 354 (2020).
6. T. Tamura et al., *Chem. Lett.*, **39**, 753 (2010).
7. T. Mandai, K. Yoshida, K. Ueno, K. Dokko, and M. Watanabe, *Phys. Chem. Chem. Phys.*, **16**, 8761 (2014).
8. Y. Yamada et al., *J. Am. Chem. Soc.*, **136**, 5039 (2014).
9. K. Sodeyama, Y. Yamada, K. Aikawa, A. Yamada, and Y. Tateyama, *J. Phys. Chem. C*, **118**, 14091 (2014).
10. S. Ko, Y. Yamada, and A. Yamada, *Joule*, **5**, 998 (2021).
11. K. M. Diederichsen, E. J. McShane, and B. D. McCloskey, *ACS Energy Lett.*, **2**, 2563 (2017).
12. Y. Yamada, J. Wang, S. Ko, E. Watanabe, and A. Yamada, *Nat. Energy*, **4**, 269 (2019).
13. K. Dokko et al., *J. Phys. Chem. B*, **122**, 10736 (2018).
14. Y. Zhang et al., *Mater. Today*, **33**, 56 (2020).
15. S. Yang et al., *J. Mater. Chem. A*, **10**, 17917 (2022).
16. Y. Chen et al., *Adv. Mater.*, **33**, 2003666 (2021), https://onlinelibrary.wiley.com/doi/full/10.1002/adma.202003666.
17. K. Chen, D.-Y. Yang, G. Huang, and X.-B. Zhang, *Acc. Chem. Res.*, **54**, 632 (2021).
18. J. Newman and K. E. Thomas-Alyea, *Electrochemical systems* (Wiley) (2012).
19. G. Kamesui, K. Nishikawa, M. Ueda, and H. Matsushima, *Electrochem. Commun.*, **151**, 107506 (2023).
20. Y. Choo, D. M. Halat, I. Villaluenga, K. Timachova, and N. P. Balsara, *Prog. Polym. Sci.*, **103**, 101220 (2020).
21. K. Obata, R. Van De Krol, M. Schwarze, R. Schomäcker, and F. F. Abdi, *Energy Environ. Sci.*, **13**, 5104 (2020).
22. M. Paunovic and M. Schlesinger, *Fundamentals of Electrochemical Deposition* (John wiley & Sons) (2006).
23. P. Bai, J. Li, F. R. Brushett, and M. Z. Bazant, *Energy Environ. Sci.*, **9**, 3221 (2016).
24. B. Horstmann et al., *Energy Environ. Sci.*, **14**, 5289 (2021).
25. G. Kamesui, K. Nishikawa, M. Ueda, and H. Matsushima, *ACS Energy Lett.*, **7**, 4089 (2022).
26. B. Boz, T. Dev, A. Salvadori, and J. L. Schaefer, *J. Electrochem. Soc.*, **168**, 090501 (2021).
27. A. Mistry, V. Srinivasan, and H.-G. Steinrück, *Adv. Energy Mater.*, **13**, 2203690 (2023).
28. K. Nishikawa, T. Mori, T. Nishida, Y. Fukunaka, and M. Rosso, *J. Electroanal. Chem.*, **661**, 84 (2011).
29. T. Nishida, K. Nishikawa, M. Rosso, and Y. Fukunaka, *Electrochim. Acta*, **100**, 333 (2013).
30. X. Xu et al., *Adv. Energy Mater.*, **10**, 2002390 (2020).
31. A. Miki et al., *J. Mater. Chem. A*, **9**, 14700 (2021).
32. A. A. Wang et al., *ACS Energy Lett.*, **6**, 3086 (2021).
33. A. Mistry and V. Srinivasan, *Joule*, **5**, 2773 (2021).
34. Y. Gao et al., *J. Energy Chem.*, **55**, 580 (2021).
35. F. R. McLarnon, R. H. Muller, and C. W. Tobias, *JOSA*, **65**, 1011 (1975).
36. F. R. McLarnon, R. H. Muller, and C. W. Tobias, *Electrochim. Acta*, **21**, 101 (1976).
37. K. Nishikawa, Y. Fukunaka, T. Sakka, Y. H. Ogata, and J. R. Selman, *J. Electroanal. Chem.*, **584**, 63 (2005).

38. H. You et al., *Chem. Phys. Lett.*, **465**, 131 (2008).
39. A. Miki, K. Nishikawa, T. Ozawa, H. Matsushima, and M. Ueda, *J. Electrochem. Soc.*, **167**, 062501 (2020).
40. K. Nishikawa, T. Saito, H. Matsushima, and M. Ueda, *Electrochim. Acta*, **297**, 1104 (2019).
41. G. Kamesui, K. Nishikawa, H. Matsushima, and M. Ueda, *J. Electrochem. Soc.*, **168**, 031507 (2021).
42. D. Anderson, J. C. Tannehill, and R. H. Pletcher, *Computational fluid mechanics and heat transfer* (Taylor & Francis) (2016).
43. M. N. Özişik, H. R. Orlande, M. J. Colaço, and R. M. Cotta, *Finite difference methods in heat transfer* (CRC press) 2nd ed. (2017).
44. K. Fujii et al., *J. Phys. Chem. C*, **117**, 19314 (2013).
45. H. Yoon, A. S. Best, M. Forsyth, D. R. MacFarlane, and P. C. Howlett, *Phys. Chem. Chem. Phys.*, **17**, 4656 (2015).
46. Y. Yamada and A. Yamada, *J. Electrochem. Soc.*, **162**, A2406 (2015).
47. J. Grondin et al., *Phys. Chem. Chem. Phys.*, **6**, 4260 (2004).
48. S. Terada, K. Ikeda, K. Ueno, K. Dokko, and M. Watanabe, *Aust. J. Chem.*, **72**, 70 (2019).
49. S. Tsuzuki et al., *Phys. Chem. Chem. Phys.*, **19**, 18262 (2017).
50. J. Fawdon, J. Ihli, F. L. Mantia, and M. Pasta, *Nat. Commun.*, **12**, 1 (2021), https://nature.com/articles/s41467-021-24297-0.
51. S. Pfeifer, F. Ackermann, F. Sälzer, M. Schönhoff, and B. Roling, *Phys. Chem. Chem. Phys.*, **23**, 628 (2021).
52. K. Ueno et al., *J. Phys. Chem. B*, **116**, 11323 (2012).